Evaluating Classification Techniques for Mapping Vertical Geology Using Field-Based Hyperspectral Sensors

Richard J. Murphy, Sildomar T. Monteiro, *Member, IEEE*, and Sven Schneider

Abstract—Hyperspectral data acquired from field-based platforms present new challenges for their analysis, particularly for complex vertical surfaces exposed to large changes in the geometry and intensity of illumination. The use of hyperspectral data to map rock types on a vertical mine face is demonstrated, with a view to providing real-time information for automated mining applications. The performance of two classification techniques, namely, spectral angle mapper (SAM) and support vector machines (SVMs), is compared rigorously using a spectral library acquired under various conditions of illumination. SAM and SVM are then applied to a mine face, and results are compared with geological boundaries mapped in the field. Effects of changing conditions of illumination, including shadow, were investigated by applying SAM and SVM to imagery acquired at different times of the day. As expected, classification of the spectral libraries showed that, on average, SVM gave superior results for SAM, although SAM performed better where spectra were acquired under conditions of shadow. In contrast, when applied to hypserspectral imagery of a mine face, SVM did not perform as well as SAM. Shadow, through its impact upon spectral curve shape and albedo, had a profound impact on classification using SAM and SVM.

Index Terms—Geology, hyperspectral imaging, minerals, mining industry, spectral analysis, support vector machines.

I. INTRODUCTION

REMOTELY sensed imagery acquired from field-based platforms is increasingly being used for a variety of applications, particularly where nondestructive measurements are required at very fine spatial scales or in areas which are too dangerous to allow direct human inspection. Most studies have, however, been done using multispectral [1], [2] or thermal imagery [3], [4]. Advances in technology now enable hyperspectral imagery to be acquired from field-based platforms, presenting new challenges and opportunities for its analysis and application. Hyperspectral imagery from field-based platforms has been mainly used for agricultural or biological applications

[5], [6]. Geological applications include mapping stratigraphy on cliff faces or in open-pit mining to map rock types and mineralogy on vertical mine walls. There have been few studies which have done applied hyperspectral imagery to these or similar applications (but see [7]).

We compare the efficacy of two classification techniques, namely, spectral angle mapper (SAM) [8] and support vector machines (SVMs) [9], to classify hyperspectral data from an open-pit iron ore mine in Western Australia. These were selected because they are suited to classifying data acquired under variable surface, illumination, and viewing geometries, either because they are insensitive to these variations (SAM) or because they can be trained to recognize them (SVM). There have been few published comparisons of the performance of these classifiers [10], and to our knowledge, there have been no studies on their relative effectiveness in classifying hyperspectral imagery acquired from field-based platforms. SAM is considered to be relatively insensitive to variations in albedo, topography, or illumination [11]–[13]. SVM is a statistical machine learning technique which has shown to be superior to conventional methods such as maximum likelihood classification [14]–[16]. SVM is less sensitive to the "curse of dimensionality" problem than other classifiers [17] and has been applied, with some success, to hyperspectral data [18]–[21]. Initially developed as a binary classifier, SVM has been modified for multiclass classification [16], [22]. SVM was selected for this study because the algorithm has the potential to "learn" the spectral effects of variable illumination geometry from training data.

Determining the effectiveness of these classification techniques is dependent upon having adequate ground truth—i.e., spectra of known samples against which the methods can be tested. Use of image data as ground truth is problematic because of mixed pixel effects or because classes within the image cannot be precisely identified or located at the required spatial resolution. Vertical mine faces are unstable, and mapping the distribution of rocks is often done from a distance and at coarse spatial resolutions, which does not allow rigorous tests of the performance of techniques. Therefore, the relative performance of SAM and SVM was first determined using libraries of field spectra of common rock types found at the mine site, thus allowing precise identification of rock classes. A "reference" spectral library, acquired in the laboratory from rock cores, was used to classify several "test" spectral libraries of rock cores and whole rock samples, acquired under different conditions of illumination, specifically under conditions of direct sunlight,

shadow, and with variable viewing geometries ($\pm 15° - 20°$ from nadir).

Using information from this analysis, SAM and SVM were then applied to hyperspectral imagery acquired from a vertical mine face, where the distribution of rock types and the position of geological boundaries were known. The objective was to use library spectra of known rock types (samples) to classify imagery of the whole mine face, thus enabling ore-bearing and non-ore-bearing rocks to be separated. In the large majority of studies, classification using SVM is done using training data extracted from the image being classified or from adjacent images (see, e.g., [10], [16], [23], and [24]). Instead, this study will use independent spectral libraries to train the SVM. This approach is crucial if hyperspectral data from any mine face within the open-pit mine are to be classified without *a priori* knowledge.

Analysis of hyperspectral imagery acquired from field-based platforms is complicated by the variable geometric relationships between the source of illumination (the sun) and the target, which itself has a complex geometry. Such surfaces reflect light in complex ways, introducing variability in brightness or color that is unrelated to mineralogy or rock type. This is a particular problem when imaging vertical surfaces from field-based platforms. Any objective comparison of the effectiveness of techniques must necessarily include analyses of the effects of changing illumination on classification. The effects of changing illumination, including shadow, on classification are evaluated by applying SAM and SVM to hyperspectral images acquired from the same mine face at different times of the day.

II. MATERIALS AND METHODS

A. Geology of the Study Area

The study area is located at the West Angelas mine in the Hamersley Province of the Pilbara Region of Western Australia. The province is characterized by extensive ($80\,000$ km^2) banded iron formation (BIF) composed of multiple layers of iron oxides, including Magnetite (Fe_3O_4) and Hematite (Fe_2O_3), with alternating bands of carbonate and chert. Supergene enrichment has formed a Martite–Goethite and Goethite iron ore deposit. Thin bands of volcanic shale are also present and act as marker horizons for exploration. Extensive beds of Shale and Manganiferous shale are also present. Mining is conducted via conventional drill and blast open-pit operations.

B. Spectral Libraries

Reflectance spectra (350–2500 nm) were acquired from the main rock types present at West Angelas (Table I) using an ASD spectrometer fitted with an 8° foreoptic. A spectrum of a calibration panel (~99% Spectralon) was acquired prior to each target spectrum. Laboratory spectra were acquired using a consistent geometry between the sensor head, target, and a halogen light source. The light source was at a distance of 30 cm from the target, at an angle of 45°. Spectra acquired under natural light were measured within 2 h of local noon (solar azimuth of 34.69°–321.87° and solar elevation of 34.08°–35.79°). The field of view of the spectrometer was 3.6 cm^2. The archived spectrum of each target area of rock was an average of 30

TABLE I
ROCK TYPES INCLUDED IN EACH SPECTRAL LIBRARY. SHALE 1
AND SHALE 2 WERE NOT SAMPLED IN T-WHOLE ROCK

Class no.	Class	Description	Ore-bearing
1	Martite	Martite – soft to hard texture. Red-brown, yellow and grey.	Yes
2	Goethite	Ochreous goethite - chalky in appearance. Yellow to brown.	Yes
3	BIF	Banded Iron Formation. Hard. High chert (silica) content.	No
4	Chert	Chert (silica). Hard. Light cream-brown to yellow.	No
5	Shale	West Angelas Shale. Soft. Pink to yellow. Kaolinitic.	No
6	Manganiferous-shale	Shale with abundant manganese. Soft. Dark brown to black. Kaolinitic. Veins of pyrolusite.	No
7	Kaolinite	Water-reactive-clay. Soft. White-pink.	No
8	Shale 1	Volcanic shale. Soft. Light cream. Kaolinitic. Used as a marker horizon.	No
9	Shale 2	Volcanic shale. Soft. Light cream. Kaolinitic. Used as a marker horizon.	No

individual spectra. All spectra were converted to reflectance and convolved to the bandpasses of the imaging sensors.

For training, a "reference" spectral library was created from samples of rock which were homogenous over an area greater than the field of view of the spectrometer (Fig. 1). To allow precise identification of rock and to provide a standard fresh surface of rock for measurement, the spectral library was created from cores of rock (10 cm wide) obtained using a diamond drill. Four separate "test libraries" of known rock samples (Table I) were created to test the performance of SAM and SVM.

1) Cores of rock measured under direct sunlight (T-sun). Spectra were measured with the sensor head oriented normal to the target.
2) Cores of rock measured under shadow (T-shadow). These spectra were spatially matched with T-sun. After the calibration panel was measured in direct sunlight, a spectrum of the rock surface was taken with the direct solar beam occluded from a distance of 2 m, casting a shadow over the surface of the sample. This library was used to assess the impact of shadow on classification.
3) Cores of rock measured from oblique viewing angles ($\pm 15° - 20°$ from nadir) under direct sunlight (T-oblique). Acquisition of spectra in this way was done to simulate changing viewing geometry/illumination on classification.
4) Whole rock samples acquired in the laboratory (T-whole rock). Rock samples were of the same rock types as in the rock cores. This library was used to test if spectra of pure rock samples from the reference library were suitable proxies for classifying spectra of whole rocks.
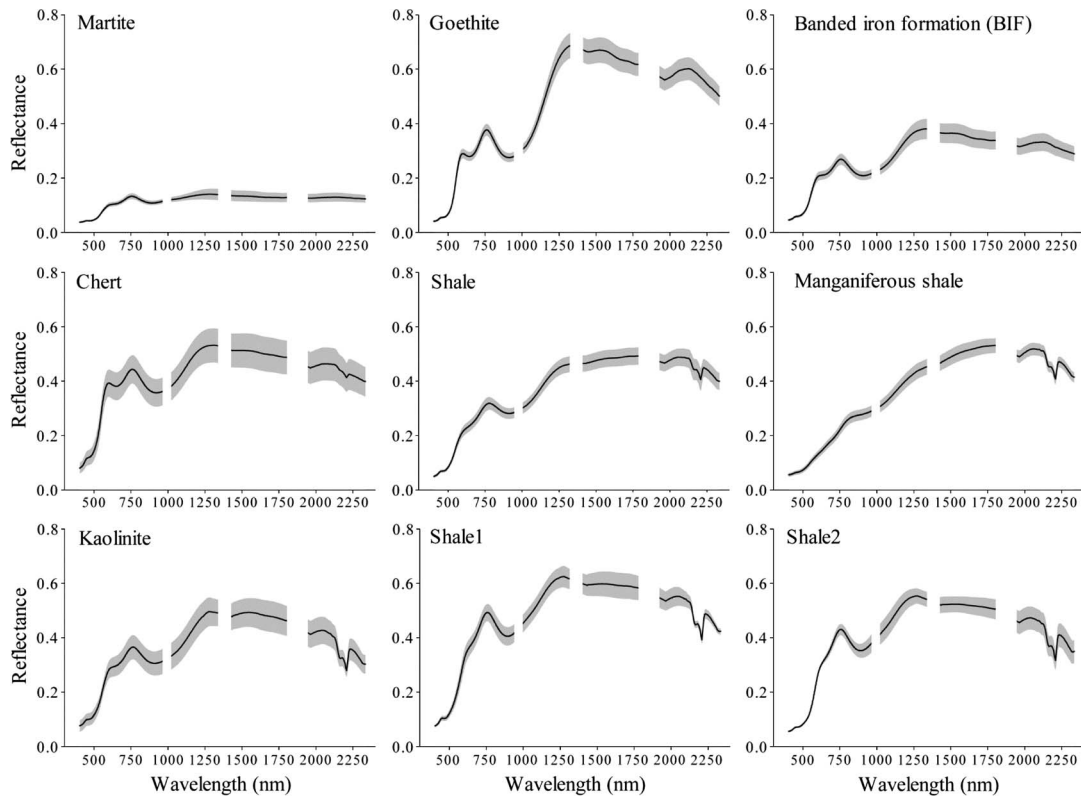
This article has been accepted for inclusion in a future issue of this journal. Content is final as presented, with the exception of pagination.

MURPHY *et al.*: EVALUATING TECHNIQUES FOR MAPPING VERTICAL GEOLOGY 3

Fig. 1.   Average spectra of rock classes in the reference library (±95% confidence interval is defined by the gray area).

C. Hyperspectral Imagery

1) Acquisition: Hyperspectral images were acquired from vertical mine faces from a distance of 30 m, using separate visible infrared (VNIR; 400–970 nm) and shortwave infrared (SWIR; 971–2516 nm) sensors (Specim, Finland) mounted adjacently on a rotating stage. The VNIR and SWIR imagers had full-width at half-maximum spectral resolutions of 2.22 and 6.35 nm, respectively. The spatial resolution (i.e., pixel dimensions) of the VNIR sensor was 6 cm, and that of the SWIR sensor was 12 cm. A calibration panel (99% reflective Spectralon; 30 cm by 30 cm) was placed next to the mine face during image acquisition. Integration time of each sensor was adjusted so that the brightest objects within the scene did not saturate.

Imagery was acquired from two mine faces. 1) A mine face which displayed several exposed geological zones characteristic of West Angelas (the "geology image"). This image was used to test how well the different methods of classification were able to distinguish geological zones on the mine face. 2) A mine face that had an orientation and geometry which experienced large variations in the angle and amount of incident illumination during the course of the day. Imagery was acquired at 11:30 A.M. ("no shadow" image) and 1:30 P.M. ("shadow" image) local time. The "shadow" image had areas of shadow which had been unshadowed in the "no shadow" image. These images were used to access the impact of shadow on the spectral signature and on classification.

2) Image Preprocessing and Calibration: A correction was applied to the spectrum at each pixel in the VNIR images to remove an artifact (an increase in reflectance toward shorter wavelengths) caused by an accumulation of charge in the detectors. Dark current was then subtracted from the VNIR and SWIR images. Each band was calibrated to reflectance by dividing it by the average of the pixels over the calibration panel and multiplying by the reflectance factor of the calibration panel [25].

Image spectra showed large increases in noise due to reduced sensor sensitivity toward the longer end of the VNIR sensor and the shorter end of the SWIR sensor (971–1027 nm) and also at wavelengths longer than 2335 nm. These spectral regions, together with wavelengths affected by atmospheric water absorption (1345–1432 nm and 1800–1962 nm), were removed, leaving 409 bands of data. The "shadow" and "no shadow" images were spatially registered using multiple ground control points.

D. Classification

1) SAM: Classification using SAM is done by assigning a class to an unknown spectrum if the angle, in multivariate space, between it and a known library spectrum is less than a certain threshold (expressed in radians). Spectra may exhibit a characteristic shape or have diagnostic absorption features, but large amounts of variability can occur among replicate spectra of the same rock type or sample [26]. Because library spectra for each rock type were collected from cores of apparently homogenous composition, one library spectrum could not be selected over another as being representative for a particular rock type. SAM was therefore implemented using all reference library spectra for each rock type. Thus, spectra of all rock types in each test library were classified by comparing them with each library spectrum for a particular rock type, i.e.,

TABLE II
SPECTRAL ANGLE (IN RADIANS) OF OPTIMAL CLASSIFICATION FOR EACH TEST LIBRARY. THE F-MEASURE AND KAPPA COLUMNS INDICATE THE
ANGLES AT WHICH SAM IS OPTIMALLY PERFORMING, MAXIMIZING THESE CRITERIA RESPECTIVELY. ASTERISKS INDICATE STATISTICALLY
SIGNIFICANT DIFFERENCES IN ANGLES FROM T-SHADOW ($P < 0.05$). Shale(M) = Manganiferous shale

Rock-type	T-sun		T-shadow		T-oblique		T-whole rock	
	F-measure	Kappa	F-measure	Kappa	F-measure	Kappa	F-measure	Kappa
Shale(M)	0.109	0.085	0.17	0.169	0.116	0.1	0.091	0.087
Shale	0.064	0.067	0.105	0.115	0.08	0.064	0.086	0.062
Goethite	0.1	0.083	0.145	0.128	0.084	0.089	0.079	0.069
Chert	0.077	0.087	0.114	0.462	0.078	0.072	0.062	0.058
BIF	0.072	0.09	0.087	0.085	0.079	0.079	0.054	0.062
Kaolinite	0.092	0.061	0.095	0.331	0.079	0.059	0.115	0.086
Martite	0.108	0.108	0.123	0.137	0.125	0.12	0.115	0.086
Shale 1	0.052	0.033	0.083	0.116	0.047	0.039	-	-
Shale 2	0.044	0.041	0.089	0.087	0.036	0.033	-	-
Average	0.079*	0.072*	0.112	0.181	0.08*	0.072*	0.093	0.078

using a "one versus all" approach. This was repeated for each rock type in the reference library until all spectra in each test library were classified. Results showed that the optimal angular threshold for classification (i.e., the angle that provided the best classification performance) varied among rock types. Statistics describing the performance of SAM were therefore generated independently for each 0.001-rad increment between 0 and 0.4 rad. The outcome of this analysis was a set of statistics that described the performance of SAM for classifying each rock type in each of the test libraries.

Classification of the test libraries showed that performance of SAM depended upon the choice of the reference spectrum. The angular threshold, which yielded the optimal classification, was found to vary among different rock types and conditions of illumination. Setting a single angle for all rock types was therefore not appropriate. SAM was therefore used to classify all images by calculating the spectral angle between the spectrum at each image pixel and *all* spectra in a spectral library formed by combining the reference and all test libraries (916 spectra in total). Classification using SAM was done in two ways. An image pixel was classified according to the following: 1) minimal angle—the class of the reference spectrum with which it had the smallest angle and 2) majority class—the majority class of the reference spectra which had the ten smallest angles with the pixel spectrum. Pixels which had an angle greater than 0.181 rad (the maximal optimal angle of classification of the test libraries; see Table II) were not classified.

2) SVM: Our implementation of SVM, outlined here, is derived from the work of Vapnik [9]. The main theoretical principle that drives SVMs is "structural risk minimization," which is a method for model selection that provides a quantitative characterization of the tradeoff between the complexity of the approximating function and the training error of the data. This theoretical result addresses the problem of overfitting and is used by SVMs to choose an optimal model complexity for a given data set. The SVM algorithm seeks to find a separating decision surface that maximizes the margin of separation between two linearly separable point sets. Furthermore, outliers and noise in the data are easily handled by using slack variables to relax the margin constraints. Details about the algorithm can be found in standard texts on SVMs (see, e.g., [27] and [29]). Our implementation uses quadratic programming to optimize the SVM [27].

To extend the algorithm to perform nonlinear classification, SVMs make use of kernel machine theory, which represents the input vectors in a high dimensional feature space, where the transformed data points become linearly separable. If the kernel function can be written as a dot product in feature space, then there is no need to calculate the feature vectors explicitly; they can be simply replaced by kernel values. This procedure— known as the "kernel trick"—is used here and corresponds to a nonlinear classification performed in the input space. The algorithm to train a nonlinear SVM is mostly analogous to the linear SVM, but in this case, the search is for a separating decision surface in feature space.

Popular choices for kernel functions are the dth degree polynomial

$$k(x, x') = (1 + \langle x, x' \rangle)^d \tag{1}$$

and the Gaussian radial basis function (RBF)

$$k(x, x') = \exp\left(-\frac{\|x - x'\|^2}{2\sigma^2}\right). \tag{2}$$

Note that a first-order polynomial kernel, $d = 1$, is a linear kernel. The RBF kernel is equivalent to mapping the input features into an infinite dimensional space. We considered other kernels that have been proposed which take into account physical characteristics of hyperspectral data (see, e.g., [30]). However, due to the somewhat mixed results reported and to allow comparison with other studies using SVMs, we decided to use the polynomial and RBF kernels in our investigation.

To perform classification, the standard procedure is to apply a hard decision function to the final SVM. We adopted an alternative approach that makes use of probabilistic estimates of class membership. Probabilistic predictions are particularly useful for problems having more than two classes, as is the case here. The decision is made based on a winner-takes-all strategy, i.e., the winning class is the one with highest probability. To obtain probabilistic estimates, we transformed the SVM output to represent the likelihood of class membership, as in [31]. The probabilities were obtained by fitting a parametric model to the output of the SVM; the parameters were calculated by the numerical optimization method proposed in [32].

Because the standard SVM performs a binary classification, modifications were required to make it applicable for multiple classes. We applied the two main approaches to solve the

multiclass problems: 1) one against all, where a classifier tests for the presence or absence of each class compared to the rest, and 2) and one against one, where the classes are grouped in pairs and a classifier is learned for each pair. We used the former to classify the spectral libraries, as it allowed direct comparison with SAM, and the latter to classify the hyperspectral images, since it produced better qualitative results. In the one-against-one approach, individual class probabilities were derived from the pairwise probabilities using a Bradley–Terry model [33]. In both approaches, once the probability estimates for each class have been calculated, the classification decision was made based on the most probable class.

3) Classification Performance: A standard set of statistics was used to determine the classification performance. For each classification, the numbers of true-positive, false-positive, true-negative, and false-negative classifications for each rock type were tabulated. From these, statistics were derived including accuracy, precision, and recall. Recall measures the quantity of positive results predicted by the classifier. It is the number of positive results predicted divided by the total number of results that should have been returned. Precision is a measure of the quality of the results predicted and is the number of positive results predicted divided by the total number of results returned [34]. Receiver operating characteristic (ROC) curves were generated from the false-positive rate (FPR) and the true-positive rate (TPR) [35]. Final comparison of the performance of SAM and SVM was done using the F-measure, which combines the information in precision and recall [36], the kappa coefficient of agreement (Kappa) [37], [38], and the area under the ROC curve (AUC-ROC) [39].

The optimal performance of SAM was defined as the spectral angle at which precision and recall intersected—the break-even point (Fig. 2). The F-measure was calculated from precision and recall at this point. The optimal performance of SAM, as measured by Kappa, was defined as its maximal value across all angles.

The images classified using SAM and SVM were analyzed quantitatively by generating statistics describing the change in classes, on a per-pixel basis, between the "no shadow" and "shadow" images. Confusion matrices were constructed showing the percentage of the total number of pixels assigned to each class in the "no shadow" image which were subsequently assigned to each class in the "shadow" image. The proportional change in the total number of pixels in each class between the "no shadow" image and the "shadow" image was calculated.

III. RESULTS

A. Classification of the Test Spectral Libraries

1) SAM: The angular threshold that yielded optimal performance in classification varied among rock types and among test libraries (see Table II and Fig. 2) and was different among performance measures. Spectra in T-shadow required a larger spectral angle than other test libraries to achieve the optimal classification performance. This was significant ($P < 0.05$ and $n = 9$) in all cases, with the exception of T-whole (Table II).

Classification performance also varied according to which reference spectrum was used. ROC curves showed that some
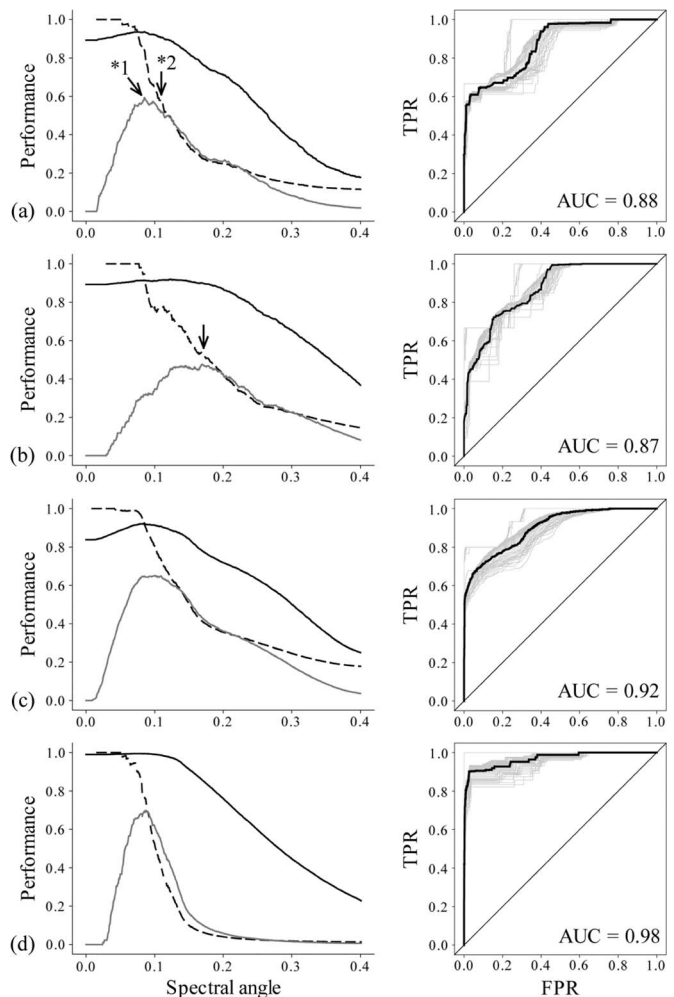

Fig. 2. Performance measures for SAM in classifying library spectra of Manganiferous shale. Left column: Accuracy (——), precision (– –), recall (·····), and Kappa (▬▬) as a function of threshold spectral angle. Right column: ROC curves of the TPR plotted against FPR. Each curve represents classification performance using a single reference spectrum. (a) T-sun. (b) T-shadow. (c) T-oblique. (d) T-whole rock. Optimal classification performance using Kappa was defined as its maximal value [arrow "∗1" in (a)]. The F-measure is calculated from precision and recall at their point of intersection [arrow "∗2" in (a)]. Note shifting of optimal classification threshold for SAM to wider angles for spectra acquired in shadow [arrow in (b)].

rock types (e.g., Goethite) showed little variation among reference spectra in the performance of classification, but other rock types showed large (e.g., BIF) or intermediate (e.g., Martite) amounts of variability (Fig. 3).

The different measures of performance for SAM for each test library gave inconsistent results (Table III). For example, in T-sun [Table III(a)], the F-measure indicated that, compared with other rock types, SAM was most successful in classifying Shale (rank = 1). However, for the Kappa and AUC-ROC performance measures, Shale was, respectively, third and fifth in the ranking. Performance statistics were also inconsistent across test libraries. SAM was more effective at classifying some rock types than others (Table III).

Taken together, these results had two major implications for how SAM was used to classify hyperspectral imagery of mine faces. First, the variability in the optimal spectral angle between libraries and rock types indicated that a single angular
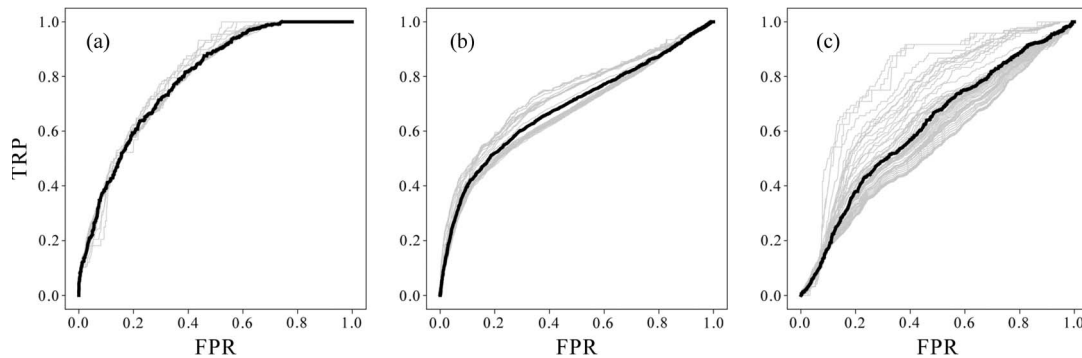
Fig. 3. ROC curves showing variability in classification performance among individual library spectra used to classify spectra using SAM. (a) Goethite. (b) Martite. (c) BIF. Black line indicates the average curve.

TABLE III
CLASSIFICATION PERFORMANCE OF SAM AND SVM (POLYNOMIAL KERNEL), MEASURED BY THE F-MEASURE, KAPPA COEFFICIENT, AND AUC-ROC FOR EACH TEST SPECTRAL LIBRARY. FOR T-WHOLE ROCK, THERE ARE NO SAMPLES FOR THE MARKER SHALES (SHALE 1 AND SHALE 2). RANKINGS (1–9) OF PERFORMANCE FOR EACH ROCK TYPE ARE SHOWN AS A PARENTHESIZED SUPERSCRIPT AFTER EACH PERFORMANCE MEASURE. Shale(M) = Manganiferous shale

a)

Rock type	F measure SAM	F measure SVM	Kappa SAM	Kappa SVM	AUC-ROC SAM	AUC-ROC SVM
Shale(M)	0.569 (5)	1.000 (1)	0.591 (4)	1.000 (1)	0.880 (3)	1.000 (1)
Shale	0.663 (1)	0.750 (4)	0.632 (3)	0.711 (4)	0.870 (5)	0.980 (3)
Goethite	0.567 (6)	0.545 (6)	0.569 (5)	0.507 (6)	0.871 (4)	1.000 (1)
Chert	0.156 (9)	0.888 (2)	0.098 (9)	0.879 (2)	0.481 (9)	1.000 (1)
BIF	0.254 (8)	0.857 (3)	0.191 (8)	0.837 (3)	0.705 (8)	0.986 (2)
Kaolinite	0.472 (7)	0.666 (5)	0.499 (7)	0.603 (5)	0.848 (6)	0.973 (4)
Martite	0.623 (2)	1.000 (1)	0.561 (6)	1.000 (1)	0.839 (7)	1.000 (1)
Shale 1	0.595 (4)	0.500 (7)	0.671 (2)	0.422 (7)	0.963 (2)	0.880 (5)
Shale 2	0.600 (3)	0.000 (8)	0.852 (1)	0.000 (8)	0.970 (1)	1.000 (1)
Overall	0.502	0.689	0.518	0.662	0.825	0.980

b)

Rock type	F measure SAM	F measure SVM	Kappa SAM	Kappa SVM	AUC-ROC SAM	AUC-ROC SVM
Shale(M)	0.529 (4)	0.800 (1)	0.475 (4)	0.781 (1)	0.874 (3)	1.000 (1)
Shale	0.591 (1)	0.000 (3)	0.585 (2)	0.000 (3)	0.951 (2)	0.890 (3)
Goethite	0.530 (3)	0.000 (3)	0.482 (3)	0.000 (3)	0.855 (4)	1.000 (1)
Chert	0.006 (9)	0.000 (3)	0.000 (9)	0.000 (3)	0.140 (9)	1.000 (1)
BIF	0.329 (6)	0.000 (3)	0.258 (6)	0.000 (3)	0.759 (5)	0.853 (5)
Kaolinite	0.066 (7)	0.000 (3)	0.034 (8)	0.000 (3)	0.421 (8)	0.893 (2)
Martite	0.362 (5)	0.333 (2)	0.279 (5)	0.125 (2)	0.739 (6)	0.880 (4)
Shale 1	0.031 (8)	0.000 (3)	0.187 (7)	0.000 (3)	0.708 (7)	0.683 (6)
Shale 2	0.588 (2)	0.000 (3)	0.655 (1)	0.000 (3)	0.965 (1)	1.000 (1)
Overall	0.377	0.126	0.328	0.100	0.712	0.9115

c)

Rock type	F measure SAM	F measure SVM	Kappa SAM	Kappa SVM	AUC-ROC SAM	AUC-ROC SVM
Shale(M)	0.688 (1)	1.000 (1)	0.650 (1)	1.000 (1)	0.918 (3)	1.000 (1)
Shale	0.634 (4)	0.833 (3)	0.635 (3)	0.808 (3)	0.886 (5)	0.986 (3)
Goethite	0.655 (2)	0.413 (7)	0.608 (4)	0.382 (6)	0.895 (4)	0.986 (3)
Chert	0.266 (8)	1.000 (1)	0.235 (8)	1.000 (1)	0.713 (8)	1.000 (1)
BIF	0.203 (9)	0.697 (5)	0.116 (9)	0.659 (5)	0.611 (9)	0.971 (5)
Kaolinite	0.485 (7)	0.758 (4)	0.561 (6)	0.739 (4)	0.878 (6)	0.980 (4)
Martite	0.617 (5)	0.963 (2)	0.520 (7)	0.952 (2)	0.828 (7)	0.999 (2)
Shale 1	0.576 (6)	0.428 (8)	0.599 (5)	0.382 (6)	0.960 (2)	0.918 (6)
Shale 2	0.640 (3)	1.000 (6)	0.641 (2)	1.000 (1)	0.980 (1)	1.000 (1)
Overall	0.529	0.788	0.507	0.767	0.852	0.982

d)

Rock type	F measure SAM	F measure SVM	Kappa SAM	Kappa SVM	AUC-ROC SAM	AUC-ROC SVM
Shale(M)	0.689 (1)	0.888 (1)	0.697 (1)	0.887 (1)	0.979 (1)	1.000 (1)
Shale	0.327 (4)	0.039 (7)	0.297 (3)	0.034 (6)	0.713 (3)	0.277 (7)
Goethite	0.347 (3)	0.359 (5)	0.275 (4)	0.289 (5)	0.793 (2)	0.871 (4)
Chert	0.070 (7)	0.075 (6)	0.028 (7)	-0.004 (7)	0.550 (5)	0.707 (6)
BIF	0.103 (6)	0.491 (4)	0.057 (6)	0.450 (4)	0.546 (7)	0.916 (3)
Kaolinite	0.168 (5)	0.610 (3)	0.045 (6)	0.536 (3)	0.359 (6)	0.759 (4)
Martite	0.581 (2)	0.809 (2)	0.306 (2)	0.698 (2)	0.668 (4)	0.957 (2)
Overall	0.327	0.467	0.243	0.413	0.658	0.783

TABLE IV
CLASSIFICATION PERFORMANCE OF SVM USING POLYNOMIAL AND RBF KERNELS FOR EACH TEST LIBRARY

Library	F measure Polynomial	F measure RBF	Kappa Polynomial	Kappa RBF	AUC-ROC Polynomial	AUC-ROC RBF
T-sun	0.689	0.792	0.662	0.771	0.98	0.982
T-shadow	0.126	0.185	0.1	0.164	0.911	0.894
T-oblique	0.788	0.796	0.769	0.778	0.982	0.978
T-whole rock	0.467	0.557	0.413	0.505	0.783	0.85
Overall	**0.52**	**0.584**	**0.49**	**0.557**	**0.922**	**0.93**

2) SVM: To classify the spectral libraries, the SVMs were applied to each rock type in a one-against-all approach, but without performing the winner-takes-all decision. The parameters for each kernel, polynomial and RBF, were optimized to maximize the averaged performance of the one-against-all binary classifiers. For the polynomial kernel, the first-degree polynomial was the best overall (Table III). The SVM using the two kernels had relatively high predictive accuracies, reaching over 90% (Table IV). Both kernels performed very closely in all metrics.

Like SAM, the different measures of performance gave inconsistent results for several rock types (Table III). SVM was more successful in classifying some rocks (e.g., Manganiferous shale) than others (Shale 1). Performance measures also varied across the different test libraries. SVM, on average, was effective at classifying T-oblique and T-sun but performed less well for T-shadow and T-whole rock.

Overall, SVM performed much better than SAM in classifying rocks from each of the test libraries. In only one case (T-shadow) did SAM give superior results to SVM, for some performance measures (F-measure and Kappa).

B. Hyperspectral Imagery—Mapping of Geological Zones

1) SAM: A contrast-enhanced true-color composite of geology image with overlaid geological boundaries and zones is shown in Fig. 4, for context. Classification using the minimal angle and majority class criteria gave similar results (Fig. 5). Shale and Manganiferous shale (Zones 1 and 2) were distinguished from rocks with greater iron content (Zones 3–7). The transition between the shales and mixed shale/ore zone is shown as an abrupt change is class from Manganiferous shale to Goethite and Manganiferous shale, coincident with the boundary mapped in the field. Zone 5 is distinguished by an increase in the number of pixels classed as Martite and

threshold could not be specified to optimally classify all rock types under different conditions of illumination, particularly under conditions of shadow. Second, variability in classification performance among reference spectra indicated that no one reference spectrum could be used as a "typical" example for any one rock type.

This article has been accepted for inclusion in a future issue of this journal. Content is final as presented, with the exception of pagination.

MURPHY *et al.*: EVALUATING TECHNIQUES FOR MAPPING VERTICAL GEOLOGY 7
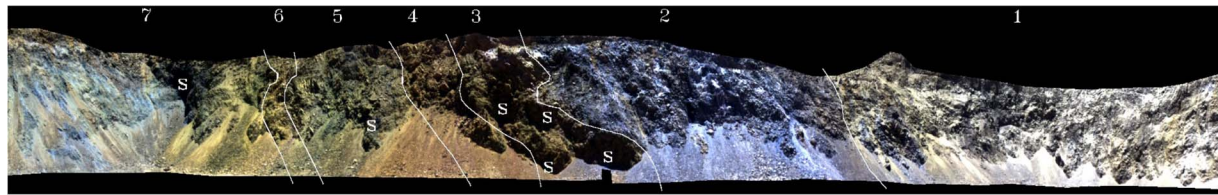

Fig. 4.   Geology image: Contrast-enhanced true-color composite with overlaid geological boundaries mapped in the field. Geological zones are indicated by numbers. (1) Shale. (2) Manganiferous shale. (3) Mixed shale and ore zone (Goethite, Shale, and Martite). (4) Ore zone (dominant Goethite with Martite background). (5) Ore zone (dominant Martite with Goethite background). (6) Ore zone (dominant Goethite with Martite). (7) Ore zone (dominant Martite with Goethite background, Chert). Shaded areas indicated by "S."
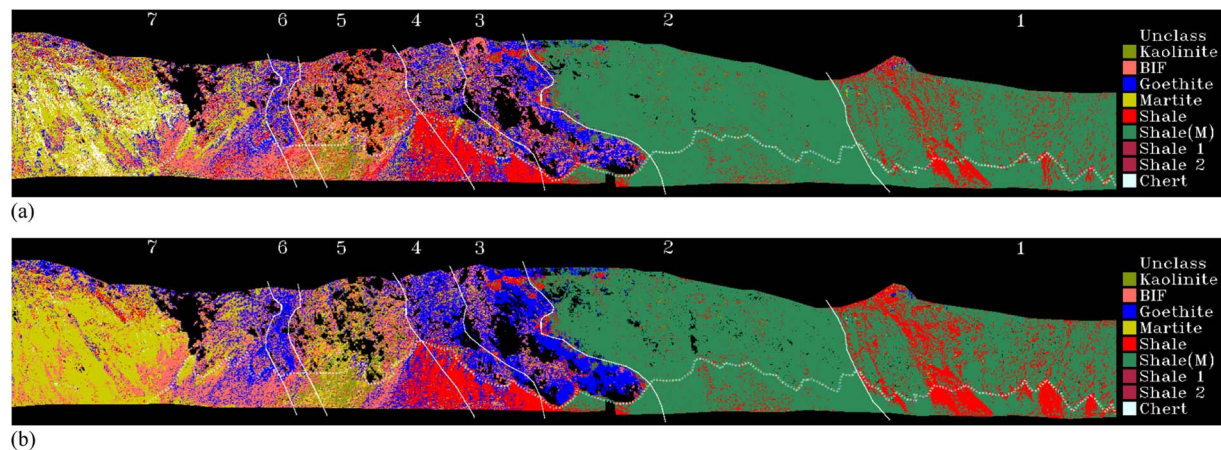

Fig. 5.   SAM classification of the geology image. The dotted line delineates boundary of the rill that has accumulated at the bottom of the mine face. Unclass = unclassified. Shale(M) = Manganiferous shale. (a) SAM (minimal angle). (b) SAM (majority class).

Kaolinite. The pixels classed as Shale in Zones 4 and 5 were observed in the field to be Shale, but they are part of the rill slope which has accumulated at the base of the face and therefore were not characteristic of the rock types native to these zones. The boundary mapped in the field between Zone 5 and the goethitic Zone 6 was delineated by a change in class from Martite/Kaolinite to Goethite. The main difference between the minimal angle and majority class images is the number of pixels classified as Chert (Zone 7).

The SAM classification agrees with the distribution of rock types as mapped in the field, indicating that the library spectra acquired from cores and whole rocks are suitable independent proxies for the bulk rock types as presented on the mine face. The percentage contribution of each spectral library in the combined library to the SAM classification using the minimal angle criterion varied (Table V). The areas left unclassified by having angles greater than 0.181 rad (the maximal angle identified from a classification of the test libraries; Table II) are coincident with the areas of shadow in the original image (cf. Figs. 4 and 5).

2) SVM: SVMs were trained using the combined spectral libraries in a multiclass framework. Preliminary experiments indicated that the one-against-one approach was faster to train and produced better results (qualitatively) than the one-against-all approach for this image, considering the number of classes. However, the SVM parameters had to be reoptimized to work on the imagery, by k-fold cross-validation of the combined spectral library. In this test, the RBF kernel performed better than the polynomial kernel.

TABLE V
PERCENTAGE CONTRIBUTION OF EACH SPECTRAL LIBRARY TO SAM CLASSIFICATION (MINIMAL ANGLE CRITERION) OF THE GEOLOGY, "NO SHADOW," AND "SHADOW" IMAGES

	Image		
Spectral library	Geology	No shadow	Shadow
Reference	36.44	9.85	11.5
T-sun	2.91	0.33	0.82
T-shadow	0.13	0.08	0.05
T-oblique	15.72	1.21	2.2
T-whole rock	44.77	88.51	85.36

Notwithstanding the good performance presented on cross-validation tests, the RBF kernel did not deliver the same good results in classifying imagery of the mine face. Contrary to expectations, the polynomial kernel performed surprisingly well. The classification using the polynomial kernel [Fig. 6(a)] agrees with SAM for some rock types (Zones 1 and 2) but not others (Zones 3–7). Unlike SAM, SVM did not delineate the different zones of ore mapped in the field. The mixed shale and ore zone (Zone 3) was incorrectly classed by the polynomial kernel as dominant Shale. The RBF kernel [Fig. 6(b)] produced a better map of some geological zones (e.g., Zone 3) than did the polynomial kernel, but not others. Zone 1, for example, was incorrectly mapped as having large amounts of Martite. Some areas of shadow in the image (location "S" on the left of the image; Fig. 4) are incorrectly classified by the RBF kernel as Kaolinite [Fig. 6(b)]. Other areas in shadow (e.g., areas of shadow in Zone 3; Fig. 4) are, however, correctly classified by the RBF as Goethite [Fig. 6(b)].
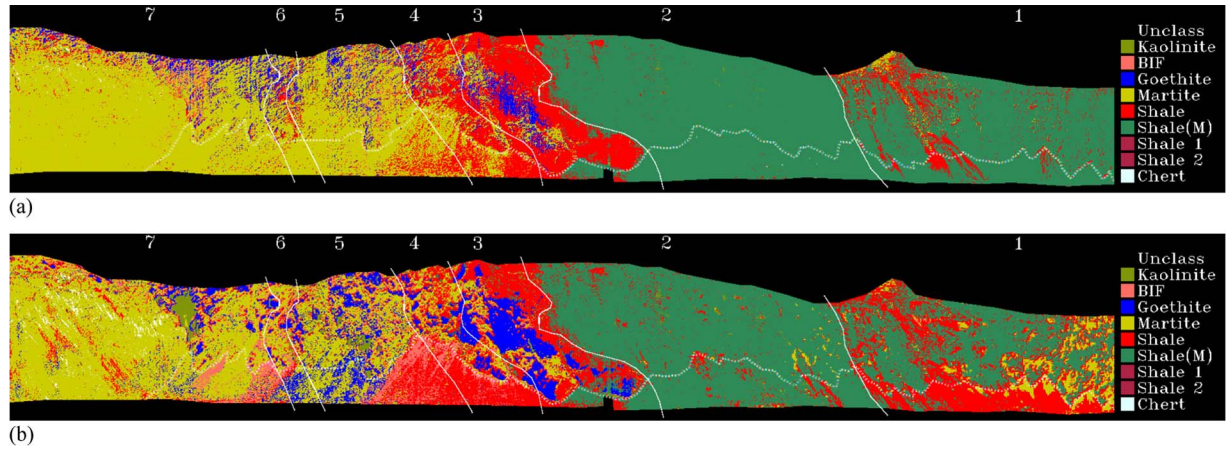
Fig. 6. SVM classification of the geology image. Unclass = unclassified. Shale(M) = Manganiferous shale. (a) First-order polynomial kernel. (b) RBF kernel.
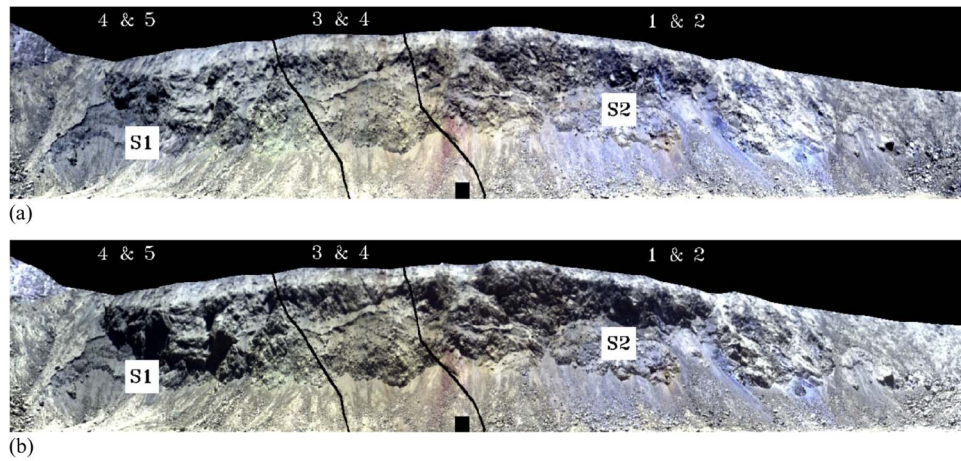

Fig. 7. Contrast-enhanced true-color composites of images acquired at different times of day: (a) "No shadow" image (11:30 local time) and (b) "shadow" image (13:30 local time). Geological boundaries mapped in the field are consistent with Fig. 4. Areas which are affected by shadow in the "shade" image are indicated by "S1" and "S2."
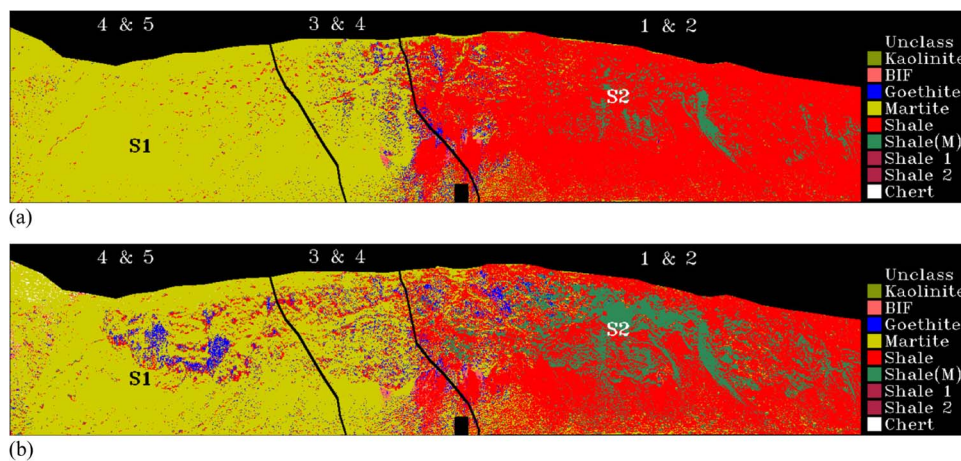

Fig. 8. SAM (majority class) classification of images acquired at different times of day. Unclass = unclassified. Shale(M) = Manganiferous shale. (a) "No shadow" image. Areas of the image, which subsequently become shadowed in the "shadow" image, are indicated by "S1" and "S2." (b) "Shadow" image. Areas of the image, which are shadowed, are indicated by "S1" and "S2."

C. Hyperspectral Imagery—Comparison of "No Shadow" and "Shadow" Images

Contrast-enhanced true-color composites show changes in illumination as localized increases in shadow (locations S1 or S2; Fig. 7) or as variations in intensity or color due to shading.

1) Differences in Classification Results Between Images: Qualitatively, SAM and SVM effectively delineated the shale zones (right) and the ore zones (left) in both the "no shadow" and "shadow" images (cf. Figs. 8 and 9). Because the SAM classifications produced using minimal angle and majority
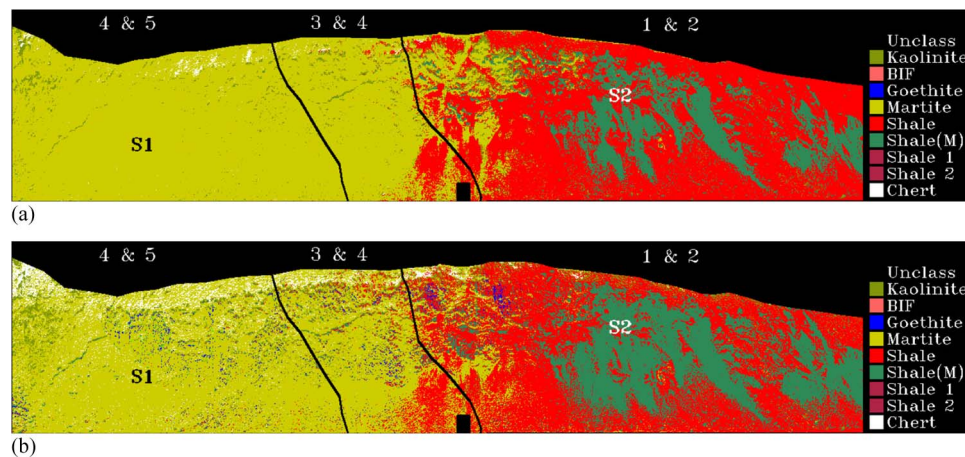
Fig. 9. SVM (first-order polynomial kernel) classification of images acquired at different times of day. Unclass = unclassified. Shale(M) = Manganiferous shale. (a) "No shadow" image. Areas of the image, which subsequently become shadowed in the "shadow" image, are indicated by "S1" and "S2." (b) "Shadow" image. Areas of the image, which are shadowed, are indicated by "S1" and "S2."

class criteria gave similar results, only the latter is shown in Fig. 8. There was an increase in small-scale spatial variability in classes ("noise") in the classified "shadow" image for the SAM and SVM classified images. Analyses showed that large numbers of pixels were assigned to a class in the "shadow" image which was different to the class they were originally assigned in the "no shadow" image (Table VI).

For SAM, the distribution and numbers of pixels assigned to each class differed markedly between the "no shadow" and "shadow" images. The most obvious changes in classification are in areas of shadow (S1 and S2; cf. Figs. 7 and 8). The dominant class near location "S1" in the "no shadow" image was Martite, but in the "shadow" image, pixels at this location were classified as Goethite [cf. Fig. 8(a) and (b)]. Similarly, at location S2 in the "no shadow" image, pixels were mainly classified as Shale, but as Manganiferous shale in the "shadow" image. Quantitative analysis of the change in classes reflects the qualitative changes observed in the images [note the increase in proportion of Goethite and Manganiferous shale pixels; Table VI(a) and (b)]. The percentage contribution of each spectral library within the combined library to the SAM classification was similar for the "shadow" and "no shadow" images, with the large majority of spectra coming from T-whole rock (Table V).

For SVM, the impact of shadow appeared to be less in the SVM than in the SAM classified image (e.g., location S1; Fig. 9). There was an increase in small-scale variability in classes, but unlike SAM, no spatially coherent change in class was observed. At location S2, however, a large number of the pixels originally classified as Shale in the "no shadow" image were reclassified as Manganiferous shale in the "shadow" image; this is consistent with the classification using SAM.

2) Links Between Changes in Pixel Class and Changes in Reflectance: Analyses were done to determine if the change in reflectance between the "no shadow" and "shadow" images was greater or smaller for pixels which changed class than for pixels which did not change class. The average reflectance at each pixel across all wavelengths was calculated separately for the "no shadow" and "shadow" images. The average reflectance

of the "shadow image" was then subtracted from the average of the "no shadow" image on a pixel-by-pixel basis, taking the absolute value. This difference was matched, at each pixel, with the SAM and SVM classified images. Pixels which remained the same class between the "no shadow" and "shadow" images had significantly smaller differences in reflectance than did pixels which changed class (Table VII).

3) Links Between Changes in Class and Changes in Shape of the Spectral Curve: The aforementioned findings and qualitative examination of the classified images indicated that spatially coherent changes in class occurred in those regions of the image which were unshadowed in the "no shadow" image but which became shadowed in the "shadow" image (locations S1 and S2 in Figs. 7 and 8). Because these changes in class were most pronounced in the SAM classification which is theoretically invariant to illumination, it was important to understand how the effects of shadow caused SAM to assign a different class to the same pixels between the "no shadow" image (where there they illuminated by direct sunlight) and in the "shadow images" (where they had become shadowed). The hypothesis was that shadow has an impact upon the shape of the spectral curve, thus causing a change in class. The change in class of pixels near location S1 was generally from Martite to Goethite, and at S2 from Shale to Manganiferous shale. Pixels which did not change class near these locations remained as Martite (S1) or Shale (S2).

Replicate pixels ($n = 5$) which did not change class or which changed class were identified near each location (S1 and S2), and their pixel spectra extracted (Fig. 10). As expected, all pixels which did not change class were found in areas which were directly illuminated by the sun in both the "no shadow" and "shadow" images, and all pixels which changed class were found in areas that were directly illuminated by the sun in the "no shadow" image but were shadowed in the "shadow" image. Spectra of pixels, which changed from Martite to Goethite, showed a distinct increase in spectral slope between the VNIR and SWIR [indicated by arrows in Fig. 10(a)]. This caused the spectrum to become more like Goethite than Martite, explaining the change in class made by SAM. The increase in spectral slope was not found in spectra which did not change

TABLE VI

PERCENTAGE OF THE *total* NUMBER OF PIXELS ASSIGNED TO EACH CLASS IN THE "NO SHADOW" IMAGE (COLUMNS) THAT HAVE BEEN ASSIGNED TO *each* CLASS IN THE "SHADOW" IMAGE (ROWS). DIAGONAL VALUES (IN BOLD) INDICATE THE PERCENTAGE OF PIXELS WHICH ARE THE SAME CLASS IN BOTH THE "NO SHADOW" AND "SHADOW IMAGES." THE LAST COLUMN SHOWS THE PROPORTIONAL CHANGE IN THE TOTAL NUMBER OF PIXELS IN EACH CLASS FROM THE "NO SHADOW" IMAGE TO THE "SHADOW IMAGE." "−" INDICATES THAT NO PIXELS FOR THIS CLASS WERE PRESENT IN THE CLASSIFIED "NO SHADOW IMAGE". Shale(M) = Manganiferous shale

a) SAM classification using minimal angle.

	Kaolinite	BIF	Goethite	Martite	Shale	Shale(M)	Shale 1	Shale 2	Chert	Prop. change
Kaolinite	**28.3**	15.9	7.91	13.3	11.66	1.29	19.4	-	5.53	0.99
BIF	2.59	**12.89**	3.82	6.88	1.17	0.2	2.99	-	3.02	0.84
Geothite	7	6.23	**26.09**	7.92	3.27	0.17	22.39	-	3.02	1.24
Martite	18.94	58.22	47.24	**64.57**	4.81	1.86	16.42	-	66.83	0.93
Shale	34.39	4.18	12.45	3.86	**56.55**	24.3	29.85	-	1.76	0.82
Shale(M)	7.18	1.59	1.9	1.05	22.5	**72.18**	8.96	-	0.5	2.30
Shale 1	0.01	0.05	0.02	0.03	0.01	0.0	**0.0**	-	0.0	0.94
Shale 2	0.0	0.01	0.01	0.0	0.0	0.0	0.0	-	0.0	-
Chert	1.05	0.93	0.57	2.38	0.02	0.0	0.0	-	**19.35**	8.70

b) SAM classification using majority class.

	Kaolinite	BIF	Goethite	Martite	Shale	Shale(M)	Shale 1	Shale 2	Chert	Prop. change
Kaolinite	**3.32**	0.16	0.4	0.35	1.47	0.09	0.0	-	0.0	0.60
BIF	1.34	**28.84**	6.7	1.54	0.83	0.04	5.76	-	14.29	3.39
Geothite	4.51	16	**16.16**	5.33	2.06	0.78	17.29	-	0.0	2.03
Martite	35.75	39.8	47.56	**83.18**	8.52	0.88	22.03	-	57.14	0.96
Shale	50.63	14.26	27.3	8.2	**70.35**	21.78	46.44	-	0.0	0.82
Shale(M)	4.21	0.39	1.28	0.79	16.62	**76.41**	7.12	-	0.0	3.74
Shale 1	0.18	0.08	0.52	0.23	0.13	0.01	**1.36**	-	0.0	1.92
Shale 2	0.0	0.0	0.02	0.0	0.0	0.0	0.0	-	0.0	-
Chert	0.08	0.47	0.07	0.39	0.01	0.0	0.0	-	**28.57**	84.14

c) SVM classification using first order polynomial kernel.

	Kaolinite	BIF	Goethite	Martite	Shale	Shale(M)	Shale 1	Shale 2	Chert	Prop. change
Kaolinite	**18.85**	-	-	6.67	4.79	0.17	-	-	6.29	1.65
BIF	0.03	-	-	0.24	0.0	0.00	-	-	0.0	368
Geothite	1.54	-	-	1.38	0.03	0.10	-	-	0.09	-
Martite	16.03	-	-	**77.24**	4.25	0.24	-	-	44.45	0.82
Shale	48.82	-	-	7.39	**70**	11.35	-	-	3.76	0.87
Shale(M)	11.67	-	-	1.63	20.55	**88.13**	-	-	0.17	1.71
Shale 1	0.0	-	-	0.0	0.0	0.0	-	-	0.0	-
Shale 2	0.0	-	-	0.0	0.0	0.0	-	-	0.0	-
Chert	0.08	-	-	5.46	0.01	0.0	-	-	**45.24**	8.4

class [Fig. 10(b)]. Pixels which changed class from Shale to Manganiferous shale similarly showed an increase in slope between the VNIR and SWIR, causing the Shale spectrum to become more like Manganiferous shale [Fig. 10(c)]. No change in slope was observed for Shale pixels which did not change class [Fig. 10(d)].

This article has been accepted for inclusion in a future issue of this journal. Content is final as presented, with the exception of pagination.

MURPHY *et al.*: EVALUATING TECHNIQUES FOR MAPPING VERTICAL GEOLOGY   11

TABLE VII
ABSOLUTE CHANGE IN REFLECTANCE (400–2335 nm) OF PIXELS WHICH HAVE REMAINED THE SAME CLASS ("NOT CHANGED")
OR WHICH HAVE CHANGED CLASS ("CHANGED") BETWEEN THE "NO SHADOW" AND "SHADOW" IMAGES.
TESTS FOR SIGNIFICANCE WERE DONE USING A STANDARD STUDENT'S t-TEST

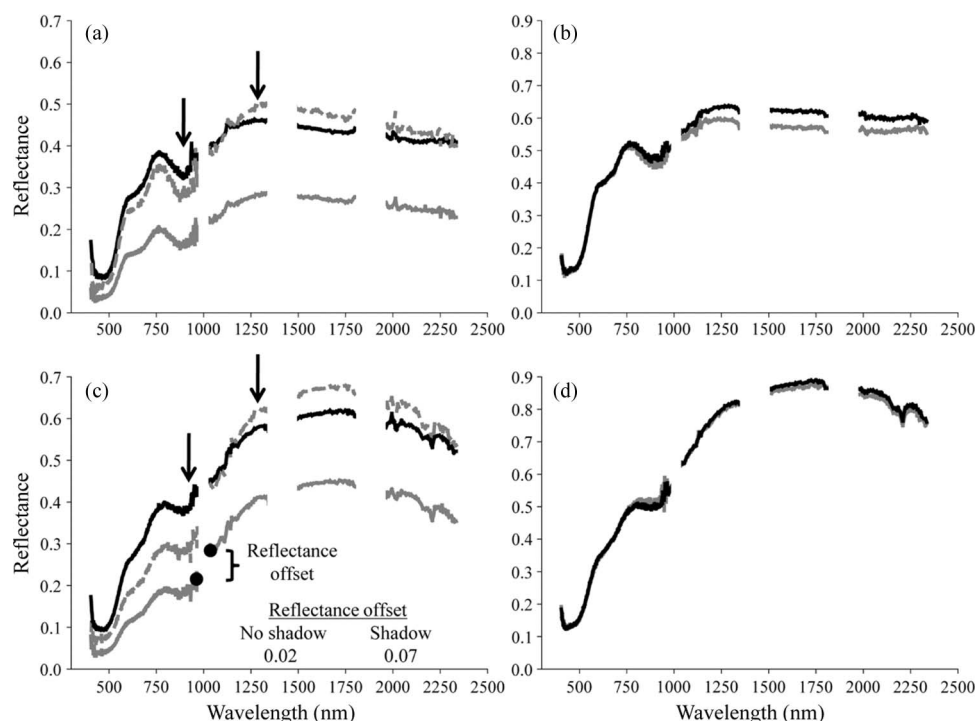|	SAM minimal angle			SAM majority class			SVM 1st order polynomial		
	Mean	SD	P	Mean	SD	P	Mean	SD	P
Not changed	0.59	0.12	< 0.001	0.61	0.20	< 0.01	0.59	0.27	< 0.05
Changed	0.94	0.15		0.86	0.30		1.16	0.56	

Fig. 10. Average spectra $(n = 5)$ from the *same* pixels near location "S1" or "S2" in the "no shadow" (——) and "shadow" (━━) images. The spectrum from the "shadow" image, rescaled to the brightness of the "no shadow" image, is shown for comparison (▬ ▬). (a) Spectra from directly illuminated pixels near "S1" which are classified as Martite in the "no shadow" image but which become shaded and classified as Goethite in the "shadow" image. (b) Spectra from pixels near "S1" which are directly illuminated in the "no shadow" and "shadow" images. Pixels are classified as Martite in both images. Note the slope of the reflectance curve that is similar for both spectra. (c) Spectra from directly illuminated pixels near "S2" which are classified as Shale in the "no shadow" image but which become shaded and classified as Manganiferous shale in the "shadow" image. The reflectance offset between the last band of the VNIR sensor and the first band of the SWIR sensor is indicated by filled circles. (d) Spectra from pixels near "S2" which are directly illuminated in the "no shadow" and "shadow" images. Pixels are classified as Shale in both images. Note the slope of the reflectance curve that is similar for both spectra.

Closer examination of the spectra indicated that the increase in slope between the VNIR and SWIR may be caused by a reflectance offset between these spectral regions [see Fig. 10(c)]. This offset is characterized by a sharp jump in reflectance from 970 nm (the last band sensed by the VNIR sensor) to 1028 nm (the first band sensed by the SWIR sensor). To determine if this reflectance offset was consistently greater for pixels which had become shadowed, ten replicate regions of interest (each 5 × 5 pixels) were extracted from areas which remained directly illuminated in both the "no shadow" and "shadow" images and, separately, from areas which were illuminated in the "no shadow" image but shadowed in the "shadow" image. The reflectance offset was significantly greater in the areas which become shadowed $(P < 0.01)$.

To determine if the increase in reflectance offset in image spectra from the "shadow" could cause the observed changes in class, the offset was simulated using library spectra of Martite and Shale. A reflectance offset was added to all wavelengths of the spectra > 970 nm, progressively in increments of 0.2%. Martite spectra with increasing offsets were matched using SAM with library spectra of Martite and, separately, Goethite. Shale spectra with increasing offsets were matched with library spectra of Shale and Manganiferous shale. With increasing offset, spectra of Martite became progressively less like Martite and more like Goethite, as indicated, respectively, by the increasing and decreasing spectral angles [Fig. 11(a)]. With increasing offset, spectra of Shale became more like Manganiferous shale. Similar results were obtained when the reflectance offset was applied multiplicatively. These findings indicate that an increase in slope (offset) between the VNIR and SWIR can cause the dominant changes in class observed between the "no shadow" and "shadow" images.

This article has been accepted for inclusion in a future issue of this journal. Content is final as presented, with the exception of pagination.

12   IEEE TRANSACTIONS ON GEOSCIENCE AND REMOTE SENSING
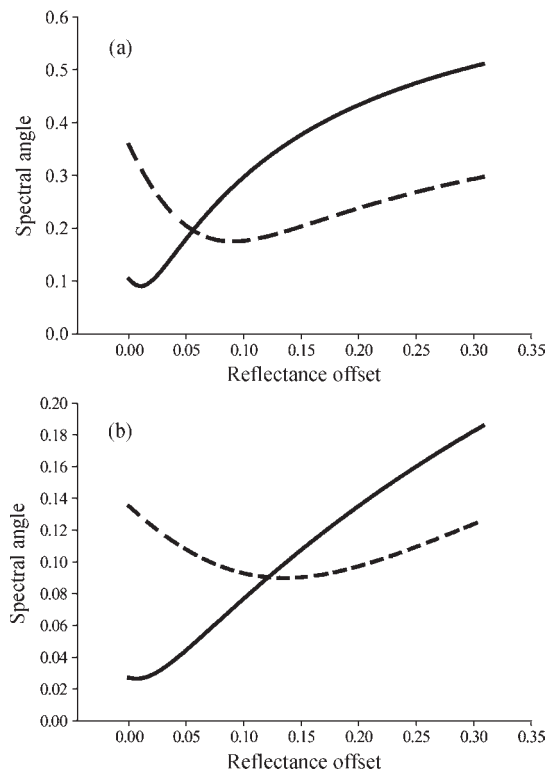

Fig. 11.   Change in spectral angle between a reference spectrum and a target spectrum to which an additive offset (in 0.2% increments) has been applied to the reflectance at SWIR wavelengths (> 970 nm). (a) Spectral angle between a Martite spectrum (with increasing reflectance offset) and, respectively, a reference spectrum of Martite (━━) and Goethite (·····). With increasing reflectance offset, the target spectrum becomes less like Martite (the spectral angle increases) and more like Goethite (the spectral angle decreases). (b) Spectral angle between a Shale spectrum (with increasing reflectance offset) and, respectively, a reference spectrum of Shale (━━) and Manganiferous shale (·····). With increasing reflectance offset, the target spectrum becomes less like Shale (the spectral angle increases) and more like Manganiferous shale (the spectral angle decreases).

IV. DISCUSSION

A. Classification of the Test Libraries

SVM consistently performed better than SAM at classifying library spectra of rocks acquired under direct sunlight or artificial illumination, supporting the conclusions of previous studies which have shown that SVM is superior to other commonly used methods of classification (see, e.g., [14] and [16]). SVM performed poorly, however, on samples for T-shadow, probably because classification of the test libraries was done using reference spectra acquired under direct illumination, not shadow. The poor F-measure and Kappa are due to the SVM classifier having zero positives in many of the T-shadow samples. Nevertheless, the high AUC-ROC values show that the SVM models are performing classification, but the standard threshold for classification (class probability greater than 0.5) does not reflect the correct distribution for those classes, thus causing the zero positives. It was not expected that SVM would be able to classify classes which were not presented during training (shadowed rocks), whereas SAM will always provide a classification on the basis of the minimal angular match with the library. Both SAM and SVM were better at classifying spectra of rock cores than spectra from whole rocks. Rock cores are free from surface coatings, and this highlights the need for selecting spectra which are representative of rocks as they present themselves on the mine face. Nearly all rocks at the mine are coated, to some degree, with goethitic dust which blurs the distinction between spectral classes.

The classification of the spectral libraries identified two limitations of SAM which had implications for how SAM was used to classify hyperspectral imagery of the mine face. First, the performance of SAM was dependent on the particular reference spectrum which was used in the classification. Second, the optimal spectral angle of classification varied among different rock types and under conditions of shadow. Thus, no single reference spectrum could be selected as a "definitive" spectrum for each class that would yield the optimal classification across different sets of data. Neither could a single angular threshold be specified which would provide the optimal classification for all rocks and under conditions of shadow. SAM was therefore applied to the images of the mine face using the minimal angle and majority class criteria. In this way, all spectra in the combined library were considered in the analysis, and no threshold had to be set *a priori*.

B. Classification of Imagery

Differences between library and image spectra may occur as a consequence of the different approaches used to calibrate them. Each library spectrum was calibrated using a calibration measurement obtained under the same conditions of illumination, thus correcting it for atmospheric absorption and changes in incident illumination. Image spectra were calibrated using a calibration panel placed within a fully illuminated part of the image. This was problematic because the complex geometry of the mine face meant that it had a range of orientations with respect to the sun; thus, some image spectra were located in areas of shadow. Our study showed that spectra in shadowed areas of the mine face have a different curve shape to spectra of pixels directly illuminated by the sun (i.e., an increase in slope between VNIR and SWIR wavelengths). Shaded pixels are illuminated by indirect light (from skylight and light reflected from the wall of the mine) which has a different wavelength-intensity distribution than direct sunlight (and, thus, the calibration panel). Indirect light would have proportionally more blue light (caused by atmospheric scattering) and more NIR light (caused by scattering of light from the goethite-rich walls and floor of the mine pit). This may account for the observed changes in the curve shape of spectra and increased reflectance offset in the shadowed areas of the mine face.

Changes in spectral curve shape due to shading caused some pixels to be classified differently in images acquired at different times of the day. This was particularly evident for SAM, where pixels classified as Martite when in direct sunlight are reclassified as Goethite when they become shadowed. Although SAM is considered to be invariant to brightness differences, the present study indicated that changes in reflectance do affect its performance. Shadow had a lesser impact on the SVM

than on the SAM classified images, probably because spectra from T-shadow were included in the training data for SVM. SAM also had "access" to all of the libraries when comparing image and library spectra; however, only a small proportion of the library spectra which had the closest match with image spectra came from T-shadow (the "no shadow" image, surprisingly, having a largest proportion). This indicates that spectra from T-shadow were not being preferentially selected in the classification of the "shadow" image. In practice, it is very difficult to construct a spectral library of shadowed spectra because their shape would be influenced by the particular environmental conditions under which they were collected (e.g., the relative amounts of absorption and scattering at each wavelength by the atmosphere and surrounding structures). The conditions under which spectra in T-shadow were collected were dissimilar to those of the mine pit at the time of image acquisition. This may explain why only a small proportion of the pixels in the image had a best match with spectra in T-shadow.

Changes in the classification of pixels between the "no shadow" and "shadow" images fell into two groups, based on the spectral absorption characteristics of the rocks. Rocks within each group tended to change classes with other members of the same group (i.e., the largest percentage changes in classification tended to occur between members of the same group). The first group contained rocks with strong ferric iron absorption features (Goethite, BIF, Chert, and Martite), and the second group contained rocks which had features associated with both iron and kaolinite (Kaolinite, Shale, Manganiferous shale, and Shale 1). Spectral variability within these groups is smaller than the variability between groups; thus, pixels change to classes within the same group rather than between groups. An inherent advantage of SAM is that it removes variations in brightness caused by variations in illumination or albedo [13]. However, this can be a disadvantage where the major discriminating factor between classes is albedo, not curve shape, as in the case for Martite and Goethite. Our data were acquired from geological surfaces which were free of surface moisture. Variability in moisture, like shade, could also have an impact on classification results. Because effects of moisture could not be assessed in the imagery, they were not considered as part of this study.

Although SVM was shown to be superior to SAM in classifying data from the test libraries, the opposite was found in the classification of the imagery of the mine face. The poor performance of the SVM in classifying hyperspectral images with a model learned from independent training data exemplifies a drawback of machine learning techniques. To obtain a high predictive accuracy, the learned model has to be tuned to the information available in the training spectra. The generality of this model when applied to new "unseen" data is hard to predict. Cross-validation was used to assess generality. In our experiments, even using parameters optimized through cross-validation, the best models did not perform as well on the images. In particular, the RBF kernel, superior in cross-validation, was outperformed by the first-order polynomial kernel on the qualitative analysis of the images, suggesting some degree of overfitting.

Although the RBF kernel is, in theory, very powerful—it provides a nonlinear transformation that has the linear kernel as a special case—it did not perform significantly better than the polynomial kernel. This is in stark contrast with previous research on SVM for hyperspectral classification that often presented RBF as the best performing kernel [21]. The poor results for this kernel suggest that a nonlinear mapping may not be necessary when the number of features is very large [41].

Another problem for SVM is a change in the distribution of the input data set from training to testing. This can be caused by problems in sensor calibration, changes in environmental conditions, or differences in sensitivity or signal-to-noise ratio between sensors. The basic assumption for the SVM approach used here is that there is no shift in the distribution of the data set from training to testing. The ideal solution would be to prevent this issue at the stage of data acquisition, but this may be only possible to a limited extent given the many factors which might affect the quality of the data. There have been methods proposed to alleviate the impact of this problem by Quinonero-Candela *et al.* [42], who suggest that a simpler model than that suggested by cross-validation can be more advantageous. Our empirical results suggest that this is the case. To learn a better model would also require the acquisition of more training data. Exploring different learning strategies to cope with data set shifts is ongoing.

V. Conclusion

The use of hyperspectral imagery to identify and map rock types on a vertical mine face using an independent spectral library has been demonstrated. Results indicate that any assessment of the performance of classification methods must take into account changing conditions of illumination. We show that variations in incident illumination, characteristic of topographically complex environments, can impact classification results, overturning established assumptions that techniques based on spectral angle (e.g., SAM) are insensitive to variations in illumination or albedo. An unexpected but significant finding of this study is that SVMs perform well when training spectra are selected from the same population of data that is being classified (i.e., both these data are acquired using the same sensor and under similar conditions) but not when they are selected from an independent library acquired with a different sensor and under different conditions. This occurred despite careful calibration of the image data to reflectance. Independent spectral libraries are central to the success of classifying hyperspectral imagery without *a priori* knowledge of a scene. SVMs, in comparison to conventional methods of classification, are known to provide superior results. This study, however, demonstrates that further work is required before SVMs can be systematically applied to imagery using independent spectral libraries.

Acknowledgment

REFERENCES

[1] R. J. Murphy, A. J. Underwood, and M. H. Pinkerton, "Quantitative imaging to measure photosynthetic biomass on an intertidal rock-platform," *Marine Ecol. Progr. Ser.*, vol. 312, pp. 45–55, Apr. 2006.

[2] A. C. Jackson, R. J. Murphy, and A. J. Underwood, "Patiriella exigua: Grazing by a starfish in an overgrazed intertidal system," *Marine Ecol. Progr. Ser.*, vol. 376, pp. 153–163, 2009.

[3] C. Hardgrove, J. Moersch, and S. Whisner, "Thermal imaging of alluvial fans: A new technique for remote classification of sedimentary features," *Earth Planet. Sci. Lett.*, vol. 285, no. 1/2, pp. 124–130, Jul. 2009.

[4] A. J. Carter, M. S. Ramsey, and A. B. Belousov, "Detection of a new summit crater on Bezymianny Volcano lava dome: Satellite and field-based thermal data," *Bull. Volcanol.*, vol. 69, no. 7, pp. 811–815, Jun. 2007.

[5] H. Okamoto and W. S. Lee, "Green citrus detection using hyperspectral imaging," *Comput. Electron. Agric.*, vol. 66, no. 2, pp. 201–208, May 2009.

[6] J. Qin, T. F. Burks, M. A. Ritenour, and W. G. Bonn, "Detection of citrus canker using hyperspectral reflectance imaging with spectral information divergence," *J. Food Eng.*, vol. 93, no. 2, pp. 183–191, Jul. 2009.

[7] T. H. Kurz, S. J. Buckley, J. A. Howell, and D. Schneider, "Geological outcrop modelling and interpretation using ground based hyperspectral and laser scanning data fusion," *Int. Archives Photogramm., Remote Sens. Spatial Inf. Sci.*, vol. 37, no. 88, pp. 1229–1234, 2008.

[8] F. A. Kruse, A. B. Lefkoff, J. B. Boardman, K. B. Heidebrecht, A. T. Shapiro, P. J. Barloon, and A. F. H. Goetz, "The Spectral Image Processing System (SIPS)—Interactive visualization and analysis of imaging spectrometer data," *Remote Sens. Environ.*, vol. 44, pp. 145–163, 1993.

[9] V. Vapnik, *The Nature of Statistical Learning Theory*. New York: Springer-Verlag, 2000.

[10] M. Lennon, G. Mercier, and L. Hubert-Moy, "Classification of hyperspectral images with nonlinear filtering and support vector machines," in *Proc. IEEE Int. Geosci. Remote Sens. Symp.*, Toronto, ON, Canada, 2002, pp. 1670–1672.

[11] C. Hecker, M. van der Meijde, H. van der Werff, and F. D. van der Meer, "Assessing the influence of reference spectra on synthetic SAM classification results," *IEEE Trans. Geosci. Remote Sens.*, vol. 46, no. 12, pp. 4162–4172, Dec. 2008.

[12] F. Tavin, A. Roman, S. Mathieu, F. Baret, W. Liu, and P. Gouton, "Comparison of metrics for the classification of soils under variable geometrical conditions using hyperspectral data," *IEEE Trans. Geosci. Remote Sens.*, vol. 5, no. 4, pp. 755–759, Oct. 2008.

[13] F. Van der Meer, "The effectiveness of spectral similarity measures for the analysis of hyperspectral imagery," *Int. J. Appl. Earth Observ. Geoinf.*, vol. 8, no. 1, pp. 3–17, 2006.

[14] G. M. Foody and A. Mathur, "Toward intelligent training of supervised image classifications: Directing training data acquisition for SVM classification," *Remote Sens. Environ.*, vol. 93, no. 1/2, pp. 107–117, Oct. 2004.

[15] M. D. Wilson, S. L. Ustin, and D. M. Rocke, "Classification of contamination in salt marsh plants using hyperspectral reflectance," *IEEE Trans. Geosci. Remote Sens.*, vol. 42, no. 5, pp. 1088–1095, May 2004.

[16] C. Huang, L. S. Davis, and J. R. G. Townshend, "An assessment of support vector machines for land cover classification," *Int. J. Remote Sens.*, vol. 23, no. 4, pp. 725–749, 2002.

[17] Y. Bazi and F. Melgani, "Toward an optimal SVM classification system for hyperspectral remote sensing images," *IEEE Trans. Geosci. Remote Sens.*, vol. 44, no. 11, pp. 3374–3385, Nov. 2006.

[18] J. A. Gualtieri and R. F. Cromp, "Support vector machines for hyperspectral remote sensing classification," in *Proc. 27th AIPRWorkshop: Adv. Comput. Assisted Recognit.*, Washington, DC, 1998, pp. 221–232.

[19] F. Melgani and L. Bruzzone, "Classification of hyperspectral remote sensing images with support vector machines," *IEEE Trans. Geosci. Remote Sens.*, vol. 42, no. 8, pp. 1778–1790, Aug. 2004.

[20] M. Pal and P. M. Mather, "Support vector machines for classification in remote sensing," *Int. J. Remote Sens.*, vol. 26, no. 5, pp. 1007–1011, 2002.

[21] A. Plaza, J. A. Benediktsson, J. W. Boardman, J. Brazile, L. Bruzzone, G. Camps-Valls, J. Chanussot, M. Fauvel, P. Gamba, A. Gualtieri, M. Marconcini, J. C. Tilton, and G. Trianni, "Recent advances in techniques for hyperspectral image processing," *Remote Sens. Environ.*, vol. 113, no. 1, pp. S110–S122, Sep. 2009.

[22] C.-W. Hsu and C.-J. Lin, "A comparison of methods for multiclass support vector machines," *IEEE Trans. Neural Netw.*, vol. 13, no. 2, pp. 415–425, Mar. 2002.

[23] A. M. Filippi and R. Archibald, "Support vector machine-based endmember extraction," *IEEE Trans. Geosci. Remote Sens.*, vol. 47, no. 3, pp. 771–791, Mar. 2009.

[24] J. A. Gualtieri, S. R. Chettri, R. F. Cromp, and L. F. Johnson, "Support vector machine classiers as applied to AVIRIS data," in *Proc. Summaries 18th JPL Airborne Earth Sci. Work-Shop*, 1999, pp. 217–227, JPL Publication 99-17.

[25] R. J. Murphy, A. J. Underwood, T. J. Tolhurst, and M. G. Chapman, "Field-based remote-sensing for experimental intertidal ecology: Case studies using hyper-spatial and hyper-spectral data for New South Wales (Australia)," *Remote Sens. Environ.*, vol. 112, no. 8, pp. 3353–3365, Aug. 2008.

[26] M. A. Cho, P. Debba, R. Mathieu, L. Naidoo, J. van Aardt, and G. P. Asner, "Improving discrimination of savanna tree species through a multiple-endmember spectral angle mapper approach: Canopy-level analysis," *IEEE Trans. Geosci. Remote Sens.*, vol. 48, no. 11, pp. 4133–4142, Nov. 2010.

[27] B. Scholkopf and A. J. Smola, *Learning With Kernals: Support Vector Machines, Regularization, Optimization and Beyond*. Cambridge, MA: MIT Press, 2002.

[28] C. M. Bishop, *Pattern Recognition and Machine Learning*, vol. 2008. Secaucus, NJ: Springer-Verlag, 2006.

[29] I. Steinwart and A. Christmann, *Support Vector Machines*. New York: Springer-Verlag, 2008.

[30] B. Guo, S. R. Gunn, R. I. Damper, and J. D. B. Nelson, "Customizing kernel functions for SVM-based hyperspectral image classification," *IEEE Trans. Image Process.*, vol. 17, no. 4, pp. 622–629, Apr. 2008.

[31] J. C. Platt, "Probabilistic outputs for support vector machines and comparisons to regularized likelihood methods," in *Advances in Large Margin Classifiers*, P. J. Bartlett, A. J. Smola, B. Schölkopf, and D. Schuurmans, Eds. Cambridge: MIT Press, 2000, pp. 61–74.

[32] H. T. Lin, C. J. Lin, and R. C. Weng, "A note on Platt's probabilistic outputs for support vector machines," *Mach. Learn.*, vol. 68, no. 3, pp. 267–276, Oct. 2007.

[33] T.-K. Huang, R. C. Weng, and C.-J. Lin, "Generalized Bradley-Terry models and multi-class probability estimates," *J. Mach. Learn. Res.*, vol. 7, pp. 85–115, Dec. 2006.

[34] D. L. Olson and D. Delen, *Advanced Data Mining Techniques*. Berlin, Germany: Springer-Verlag, 2008.

[35] T. Fawcett, "An introduction to ROC analysis," *Pattern Recognit. Lett.*, vol. 27, no. 8, pp. 861–874, Jun. 2006.

[36] C. J. van Rijsbergen, *Information Retrieval*. London, U.K.: Butterworth, 1979.

[37] R. G. Congalton, R. G. Oderwald, and R. A. Mead, "Assessing Landsat classification accuracy using discrete multivariate-analysis statistical techniques," *Photogramm. Eng. Remote Sens.*, vol. 49, no. 12, pp. 1671–1678, 1983.

[38] W. D. Hudson and C. W. Ramm, "Correct formulation of the Kappa coefficient of agreement," *Photogramm. Eng. Remote Sens.*, vol. 53, no. 4, pp. 421–422, 1987.

[39] W. J. Krzanowski and D. J. Hand, *ROC Curved for Continuous Data*. London, U.K.: Chapman & Hall, 2009.

[40] E. A. Ashton, B. D. Wemett, R. A. Leathers, and T. V. Downes, "A novel method for illumination suppression in hyperspectral images," in *Proc. SPIE*, 2008, pp. 69 660C-1–69 660C-8.

[41] Y.-W. Chang, C.-J. Hsieh, K.-W. Chang, M. Ringgaard, and C.-J. Lin, "Training and testing low-degree polynomial data mappings via linear SVM," *J. Mach. Learn. Res.*, vol. 11, pp. 1471–1490, Mar. 2010.

[42] J. Quinonero-Candela, M. Sugiyama, A. Schwaighofer, and N. D. Lawrence, *Dataset Shift in Machine Learning*. Cambridge, MA: MIT Press, 2009.

Richard J. Murphy received the B.Sc. degree from University College London, London, U.K., in 1988 and the Ph.D. degree from the University of Reading, Berkshire, U.K., in 1993.

At the University of Reading, his research was on the effects of vegetation on the hyperspectral signature of soils and minerals. At Plymouth Marine Laboratory, Plymouth, U.K., his contribution to the Land–Ocean Interaction Study (LOIS), from 1993 to 1995, was to develop algorithms to derive chlorophyll and suspended sediment concentration from remotely sensed data of coasts and estuaries. Appointed to the position of Scientist with the National Institute of Water and Atmosphere, New Zealand, he developed and led New Zealand's Ocean Colour Programme, from 1995 to 1999. He is currently a Senior Research Fellow with the University of Sydney, New South Wales, Australia, where he has developed multispectral and spectroscopic methods for quantifying and characterizing intertidal biofilms *in situ*. His current work at the Australian Centre for Field Robotics, University of Sydney, involves the use of field-based sensors for geological applications.

Sildomar T. Monteiro (M'06) received the M.Sc. degree in computer science from the Aeronautics Institute of Technology, Sao Jose dos Campos, Brazil, in 2002 and the Ph.D. degree in engineering from the Tokyo Institute of Technology, Tokyo, Japan, in 2007.

After receiving his degree, he was awarded a postdoctoral fellowship from the Japan Society for the Promotion of Science and worked as a Visiting Researcher with the same institute. Since 2008, he has been with the academic staff at the University of Sydney, Sydney, Australia, where he is currently a Research Fellow with the Australian Centre for Field Robotics. His research interests lie in machine learning, statistical signal and image processing, and their applications, particularly in robotics, remote sensing, and biomedical engineering.

Dr. Monteiro is a member of the IEEE Geoscience and Remote Sensing Society.

Sven Schneider received the Diplom-Engineer degree in photonics and image processing from the University of Applied Sciences, Darmstadt, Germany, in 2008. He is currently working toward the Ph.D. degree at the Rio Tinto Centre for Mine Automation.

He joined the Australian Centre for Field Robotics, University of Sydney, Sydney, Australia, in 2009, as an Engineer for hard- and software development. His field of research is classification of hyperspectral data using machine learning. His research interests include pattern recognition, remote sensing, multi/hyperspectral image processing, and medical imaging.